Enhanced secondary pollution offset reduction of primary emissions during COVID-19 lockdown in China

Xin Huang[1*], Aijun Ding[1*], Jian Gao[2*], Bo Zheng[3,4*], Derong Zhou[1], Ximeng Qi[1], Rong Tang[1], Chuanhua Ren[1], Wei Nie[1], Xuguang Chi[1], Jiaping Wang[1], Zheng Xu[1], Liangduo Chen[1], Yuanyuan Li[1], Fei Che[2], Nini Pang[2], Haikun Wang[1], Dan Tong[3,5], Wei Qin[6], Wei Cheng[6], Weijing Liu[7], Qinyan Fu[8], Fahe Chai[2], Steven J. Davis[3,5], Qiang Zhang[3], Kebin He[3,4]

[1]School of Atmospheric Sciences, Nanjing University, Nanjing, 210023, China
[2]Chinese Research Academy of Environmental Sciences, Beijing, 100012, China
[3]Department of Earth System Science, Tsinghua University, 100084 Beijing, China;
[4]State Key Joint Laboratory of Environment Simulation and Pollution Control, School of Environment, Tsinghua University, 100084 Beijing, China
[5]Department of Earth System Science, University of California, Irvine, Irvine, CA, USA.
[6]Jiangsu Environmental Monitoring Center, Nanjing, 210036, China.
[7]Jiangsu Provincial Academy of Environment Science, Nanjing 210036, China.
[8]Shanghai Environmental Monitoring Center, 200030 Shanghai, China;
*These authors contributed equally to this work. Correspondence and requests for materials should be addressed to A. D. (dingaj@nju.edu.cn.) or Q. Z. (qiangzhang@tsinghua.edu.cn).

In order to control the spread of the 2019 novel coronavirus (COVID-19)[1,2], China imposed nationwide restrictions on the movement of its population (lockdown) after the Chinese New Year in January of 2020, leading to large reductions in economic activities and associated emissions[2,3]. However, despite such large decreases in primary pollution[3], there were nonetheless several periods of heavy haze pollution in East China during the COVID-19 lockdown, raising questions about the well-established relationship between human activities and air quality[4]. Here, using comprehensive in-situ measurements and chemical transport modeling, we show the haze events during the COVID lockdown were driven by enhancements of secondary pollution. In particular, large decreases in NO_x emissions from transportation increased ozone and nighttime NO_3 radical formation, and these increases in atmospheric oxidizing capacity in turn facilitated the formation of secondary inorganic and organic particulate matter. Our results, afforded by the tragic natural experiment of the COVID-19 pandemic, indicate that mitigation of Chinese haze pollution may depend upon a coordinated and balanced strategy for controlling multiple pollutants.

Efforts to control the spread of the 2019 novel coronavirus (COVID-19) have drastically reduced human activities worldwide[1,2]. As the epicenter of the pandemic, China was the first country to shut down commercial activities, restrict travel, and require its people to stay home beginning in late January 2020[1,3,4]. These restrictions

are believed to have drastically decreased air pollutant emissions. For example, the TROPOMI instrument on the Sentinel 5P satellite observed approximately 65% decrease in tropospheric NO_2 columns over eastern China region compared to the same period in 2019[3]. Previous studies have shown that heavy haze pollution in eastern China has primarily been driven by accumulated anthropogenic emissions together with rapid secondary production[5-11]. Indeed, strict policies reduced anthropogenic air pollution emissions in China between 2013-2017 have been the main driver of decreases in $PM_{2.5}$ pollution (concentration of particles with an aerodynamic diameter smaller than 2.5 µm) in the country[12-14].

Yet despite large reductions in primary pollutant emissions, there were several heavy haze events over eastern China during the COVID-19 lockdown, which have seeded doubt among the Chinese public and policymakers regarding the current scientific understanding of the mechanisms of haze pollution. Here, using comprehensive measurements of the mass and chemical compositions of $PM_{2.5}$ as well as related trace gases, together with numerical model simulations, we show that secondary pollution during the COVID lockdown was unexpectedly enhanced as the result of imbalances in the reduction of primary emissions. Our findings thus underscore the importance of a carefully tailored and balanced strategy of emission control to reduce haze pollution in China.

Fig. 1 and Extended Data Fig.1 show the large change in pollutant emissions during the three weeks of the Chinese New Year holiday and the COVID lockdown that immediately followed (the lock period) in comparison with three weeks before the Chinese New Year (pre-period), based on the real-time measurement by air quality monitoring network. Nitrogen dioxide (NO_2) levels decline sharply (by >60%) during the lockdown, consistent with both the reduction in human activities reflected by the transportation index (Figs. 1a, 1e) and satellite observations (Extended Data Fig. 2)[3]. Other primary gaseous pollutants such as carbon monoxide (CO) and sulfur dioxide (SO_2) show patterns similar to NO_2 (Extended Data Fig. 1). Yet concentrations of $PM_{2.5}$—perhaps the most important air pollutant from a public health perspective—do not show the same decrease over eastern China, but instead increase in the area of Beijing, Tianjin and Hebei (BTH) and in the northern part of China (Figs. 1b, 1e). Meanwhile, ozone (O_3), which is an important secondary pollutant in warmer months but generally of less concern in winter[15,16], was also substantially enhanced (in some cases by >100%) over all of eastern China (Fig. 1e). The distribution of pollutant levels shows systematic shifts in O_3 and NO_2 in the heavily populated BTH and Yangtze River Delta (YRD) areas of eastern China during the COVID lockdown, with less change in $PM_{2.5}$, particularly in the BTH region (Extended Data Fig. 3). The ratio of $PM_{2.5}$/CO, an indicator of secondary formation to primary emission, reveals a large-scale enhancement throughout northern China (Fig. 1d). The anomalies in all these species diminish near the end of February, when COVID restrictions began to be eased and people outside of the Hubei province started back to work (Fig. 1e)[1].

The observed changes in primary pollutants are proportionate to reductions in emissions during the COVID lockdown. Emissions estimates based on up-to-date activity levels suggest an overall reduction of NOx about 60-70% in eastern China, 70-80% of which was related to road traffic and 20-25% from industry and power plants (Extended Data Table 1). Model simulations with fixed emission inventory (to exclude the possible influence of synoptic weather on air pollution)[4,17,18] show the same reduction in primary pollutants and elevated O_3 and $PM_{2.5}$, especially in the BTH region (Extended Data Fig. 4). Importantly, studies of previous changes in pollution emissions have never found such a pronounced increase in secondary pollutants like O_3 and $PM_{2.5}$[19-23]. But the reduction in primary pollutants during the COVID lockdown are also more extreme than those observed previously (e.g., during past holidays or special events such as the 2008 Olympics or the 2014 meeting of the Asia-Pacific Economic Cooperation in Beijing)[19,24-27].

Prior studies have suggested many different processes of secondary PM formation in northern China[5-11]. To investigate the causes for the increase in $PM_{2.5}$ in eastern China during the COVID lockdown, we examine the chemical compositions of $PM_{2.5}$ from a regional network in northern and eastern China. Because elemental carbon (EC) is mainly from primary emissions[28,29], the relative concentration of secondary species, e.g. sulfate, nitrate, ammonium, and organic matter, provides information on secondary PM formation. As shown in Fig. 2a, secondary aerosol production during the lockdown was especially high in eastern China in comparison to the pre-period, especially in the BTH region (with a ratio of $\Delta SNAO/\Delta EC$ as high as 1.5). Such secondary formation is also consistent with the $PM_{2.5}/CO$ ratios from the air quality monitoring network (Fig. 1d). The scatter plots of the $\Delta SNAO/\Delta EC$ during the lockdown indicate an overall reduction in EC for all station (the ratio of $EC_{lock/pre}$ lower than 1 with a minimum as low as 0.4), but a substantial enhancement in secondary PM formation, shown by the much higher ratio of $\Delta SNAO/\Delta EC$ $_{lock/pre}$ (Figs. 2b-d). For sulfate and OM, the ratio is particularly high, about 20%~ 100% (Figs. 2b, 2d), but for nitrate, the ratio is relatively low (-30%~60%), with some cities in the YRD below the 1:1 line (Fig1. c), indicating weakened nitrate formation. However, for the BTH region all secondary inorganic aerosols, e.g. sulfate, nitrate (and ammonium), and organics show significantly higher net chemical production (see the ratio of $SNAO_{lock/pre}$ over 1.0, marked in red), thereby a pretty high concentration of $PM_{2.5}$ in the northern China in Fig. 1.

The diurnal cycle of the $\Delta SNAO/\Delta EC$ $_{lock/pre}$ ratio further reveals the main processes that influence secondary PM. As that shown in Extended Data Fig. 5c, the secondary production of all aerosol species in the BTH area were enhanced (positive values) most of the day during the lockdown period, with the enhancement extending from midnight to around 9:00 LT(local time) in the morning. The enhancement of secondary aerosols coincides with the rise in ozone (over 100%) and also O_3*NO_2, a proxy of NO_3 radical, which is a vital oxidant for nighttime secondary aerosol formation[30-34]. However, in other regions, such as YRD, the diurnal cycle of these ratios shows an overall positive value, except for nitrate, which was consistent with the change of O_3*NO_2 proxy

(Extended Data Fig. 5d). These results imply that—although secondary haze formation was generally enhanced during the COVID lockdown—the magnitude of such secondary aerosol production was different in different regions, depending on O_3 and the NO_3 radical. This suggests the great importance of NOx on both daytime and nighttime atmospheric chemistry[31,35-38].

We further conduct model simulations using the Weather Research and Forecasting model coupled with chemistry (WRF-Chem), based on an up-to-date emissions inventory estimated by dynamically-adjusted human activity levels (Extended Data Table 1; Extended Data Fig. 6). As aforementioned, we find significant decreases in atmospheric NO_x, due mainly to lower vehicle emissions, could cause a substantial increase in the availability of O_3 and nighttime NO_3 radical in eastern China (Fig. 3). Moreover, the simulations reproduce the enhancements of both O_3 and NO_3 radical in eastern China, a region with intensive anthropogenic emissions of NOx [39,40], and a decrease in southern and southwestern China (Fig. 3a and Extended Data Fig.7). The diurnal cycles from both model simulations (Fig. 3b) and observation-based diagnose (Extended Data Fig. 5) show that although the daytime increase were stronger but because of a stronger NO-titration effect existed in high NO environment in winter[37,38] [15], particular in the northern China, the relative change in O_3 are relatively substantial in nighttime (Fig. 3b, Extended Data Fig. 7). Accordingly, the NO_3 radical increased a lot below the altitude of 1 km during the night, even if its precursor NOx declined sharply. The enhanced atmospheric oxidizing capacity accelerated the formation of sulfuric acid (H_2SO_4) in the boundary layer[41,42]. Comparatively, such kind of enhancement are much stronger in BTH region than the YRD region.

By diagnosing the changes in HNO_3 and nitrate in WRF-Chem simulations (Extended Data Fig. 8), we can explain the differences in diurnal cycle of nitrate changes in BTH and other regions (Extended Data Fig. 5). In the BTH region, a substantial increase of HNO_3 occurs in the boundary layer almost the entire day with a positive nitrate formation occurring from night to early morning in the lower PBL. However, in the YRD region HNO_3 and nitrate show an overall decrease during the COVID lockdown (Extended data Fig. 8), consistent with observations (Fig. 2c, Extended Data Fig. 5f). As a result of the enhanced oxidizing capacity, the model shows a significant increase in sulfuric acid production during the daytime in eastern China (Fig. 3 and Extended Data Fig. 8). Observations at the SORPES station in Nanjing also show an increase in sulfuric acid concentration (~30 % increase) in both day and night (Extended Data Fig. 9). Consequently, vigorous new particle formation processes and stronger sulfate production were frequently observed at the station during the COVID lockdown. It also worth noting that a substantially higher OM fraction at night during the lockdown period was associated with stronger daytime NPF events (Extended Data Fig. 9), implying that the enhanced formation of secondary aerosols was due to a stronger nighttime oxidization by both O_3 and NO_3 racial[31,32,43], even under the condition of decreasing precursors (i.e., VOCs, SO_2, and NOx). Extended Data Fig. 10 illustrates such non-linear relationship of reduced precursors causing enhanced oxidants and

secondary products.

The non-linear relationship between NOx reduction and oxidant enhancement is also evident in measurements from air quality monitoring networks. As shown in Extended Data Fig. 11, the relationship of O_3 and night O_3*NO_2 proxy vs. NO_2 in BTH and YRD regions shown distinct patterns during the COVID-lock and pre-COVID periods. A more substantial enhancement of oxidizing capacity, for both O_3 and NO_3 radical, took place in BTH region. By testing the sensitivity of our WRF-Chem simulations to different NOx reduction rate (from 10%-90%), we find a non-linear response in both O_3 and NO_3 radical in eastern China (Fig. 4). These results show that the sudden and precipitous reduction in NO_x emissions could cause a substantial increase of O_3, NO_3 radical and hence a non-linear response of oxidation products like H_2SO_4, HNO_3, and N_2O_5 and oxygen-containing organic compound. In BTH region, the enhancement is extremely significant because of the much higher NO_x concentrations and weak incident solar radiation in northern China, which makes the NO-titration and O_3-VOCs-NO_x photochemistry more sensitive to the NO_x reduction[37]. Fig. 4 also suggests that a further reduction of NO_x (e.g., to 60%-70% in BTH and 50-60% in YRD, achieved from industrial or residuals sectors[44]) would reach a tipping-point for decreasing oxidizing capacity. Unfortunately, the emission reductions in both regions during the COVID lockdown were almost at the peak for secondary production. A concurrent reduction in VOCs could also have reduced the non-linear relationship. As that shown in Extended Data Fig. 12, synchronous VOCs reduction could have partly counterbalanced the enhancement of secondary pollution due to such non-linear response.

Our results show that the dramatic reductions in NO_x and other air pollution emissions during China's COVID lockdown led to substantial increases in O_3, which in turn increased atmospheric oxidizing capacity and enhanced formation of secondary aerosols in eastern China. In China, winter haze and summer ozone pollution are the two major air quality challenges, but with different and separated control policies. To mitigate haze pollution, policies have focused on the reduction of primary emissions such as SO_2, NO_x, and NH_3[12,45,46], while proposed efforts to reduce ozone pollution target VOCs[16]. Although regulation of SO_2 and NO_x emissions imposed since 2013 have successfully reduced haze pollution in eastern China[12,13], our results suggest that the benefit of proposed further reductions in primary emissions[44,47,48] might be offset by enhanced secondary formation of PM. Thus, the lockdown imposed to protect public health during the COVID pandemic has shown that efforts to further decrease $PM_{2.5}$ pollution in eastern China may be more challenging than anticipated. Specifically, a non-linear tipping-point of NOx chemistry will require that future reductions in China's haze pollution manage the balance of emitted species, with different consideration of VOCs and NOx ratios among different regions.
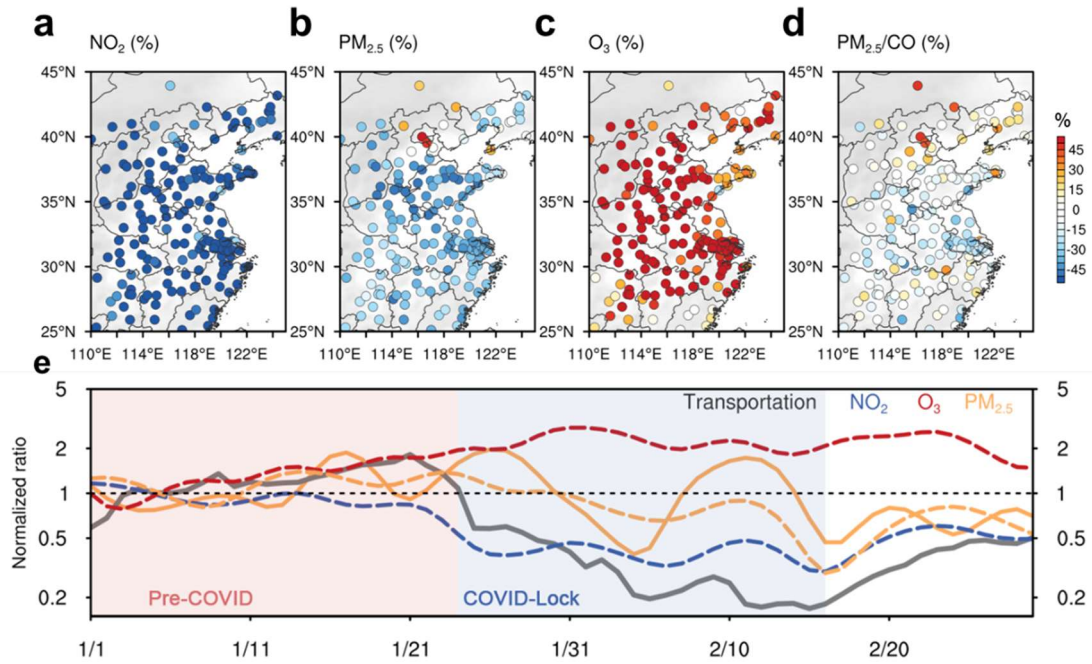
Fig. 1 | Changes in air quality before and during the COVID-19 lockdown in eastern China. a - d Differences in averaged concentrations of NO_2, $PM_{2.5}$, O_3 and $PM_{2.5}/CO$ ratio before (1-24 January, 2020) and during (26 January -17 February 2020) the COVID-19 lockdown periods at air quality monitoring stations in eastern China. **e,** Time series of normalized change in NO_2, O_3, $PM_{2.5}$ in eastern China (30 °N-40 °N, 110 °E-120 °E) and transportation index in China in January – February 2020. Note: The normalized ratio is calculated using time series with daily variation removed by EEMD filter and scaled with the first 10-day average.
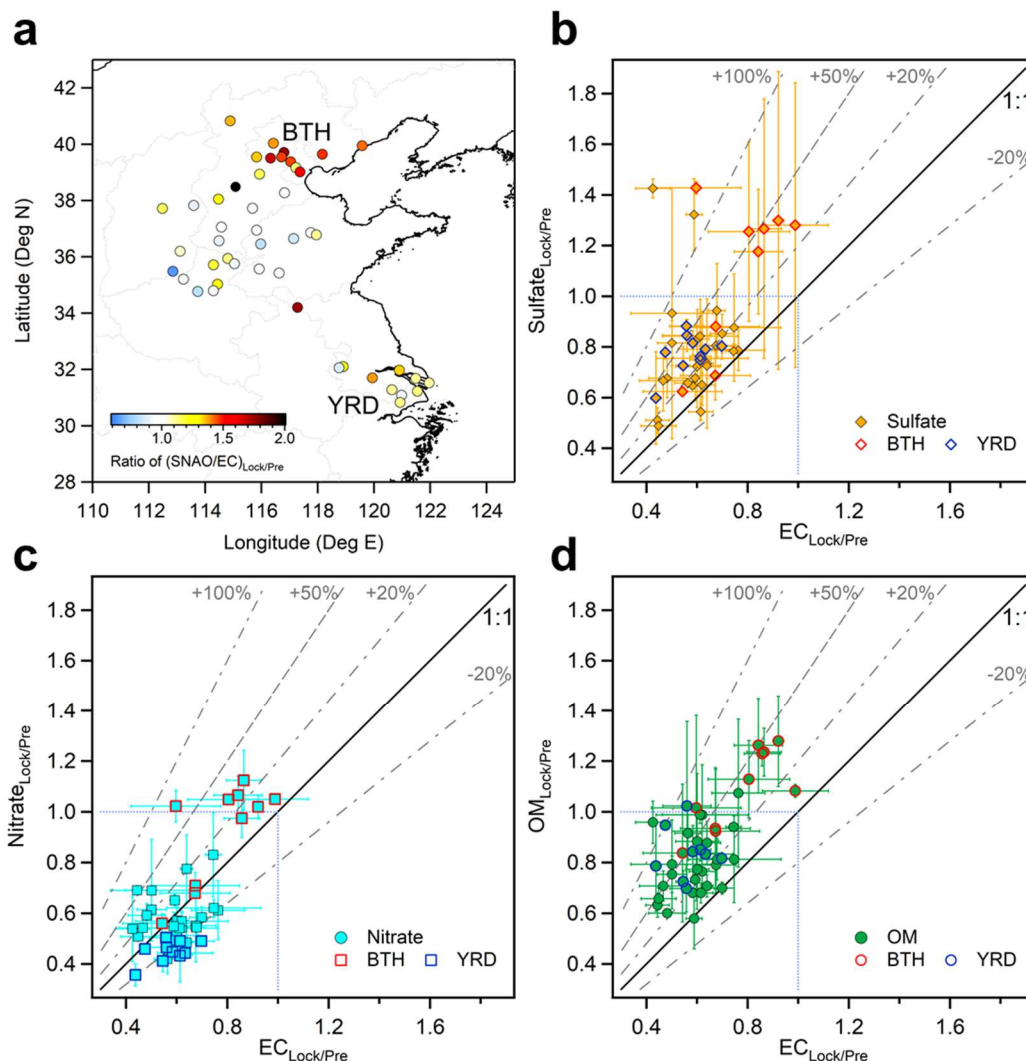
Fig. 2 | Observational evidences of enhanced secondary PM production in eastern China during the COVID-19 period. a, Spatial distribution of the ratio of total secondary PM (sulfate, nitrate, ammonium and organic matters) verse element carbon (EC), i.e. $(SNAO/EC)_{lock/pre}$, between the COVID-lock and pre-COVID period. **b-d,** Scatter plots of the ratios of sulfate, nitrate, and organic matters during COVID-lock verse pre-COVID period as a function of the ratio of EC during the two periods. Note: Error bars present the standard deviations. Data of cities in the BTH and YRD regions are marked in red and blue edge line.
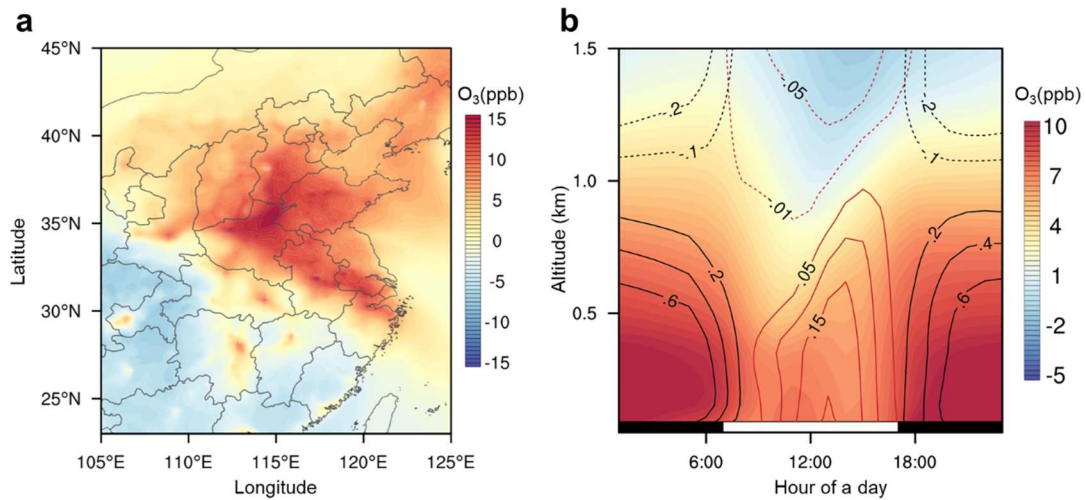
Fig. 3 | Modeling evidences of enhanced oxidizing capacity in eastern China due to the COVID-19 lockdown. a, Spatial distribution of averaged ozone enhancement by emission reduction due to the COVID-19 outbreak. **b**, Diurnal cycle of averaged vertical distribution of O_3, NO_3 radical and sulfuric acid in eastern China (30 °N-40 °N, 110 °E-120 °E). Note: Black lines mean the contour of NO_3 radical (Unit: pptv), and red lines present that of sulfuric acid (Unit: pptv). The black and white bar near the x axis in **b** indicates the nighttime and daytime of a day.
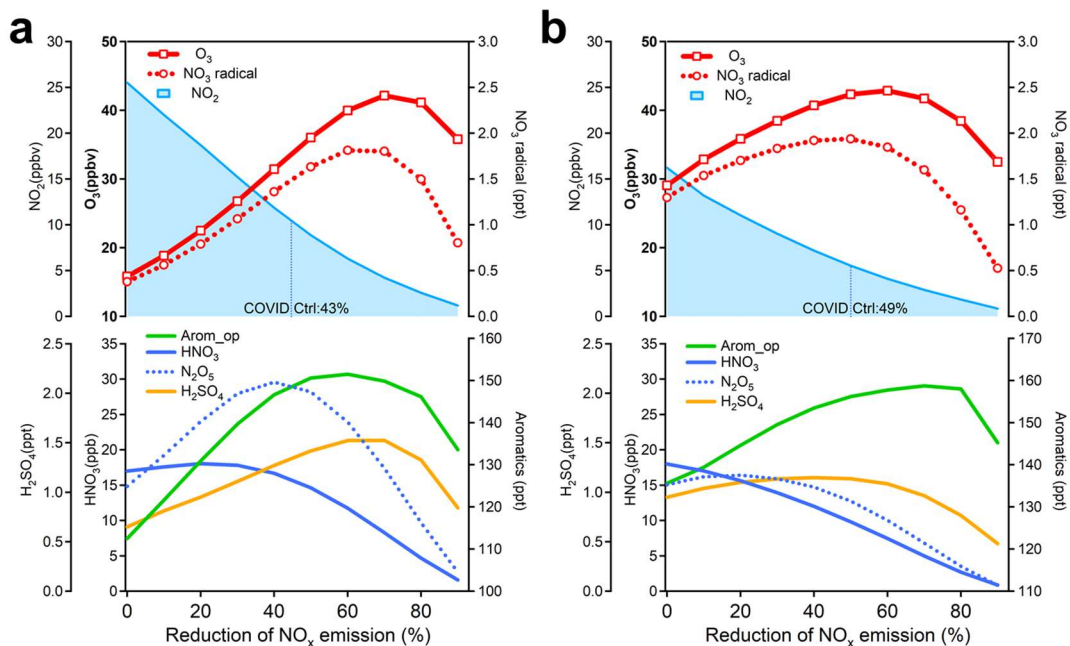
Fig. 4 | Response of oxidizing capacity to NOx emission reduction in the BTH and YRD, China. a, b, Changes of NO_2, O_3, and NO_3 radical (upper panel) and gaseous products (proxy) (lower panel) as a function of emission reduction in the BTH and YRD regions, respectively. Note: BTH and YRD are defined as the domains of (36˚N-40˚N, 114˚E-118˚E) and (29-33˚N, 118˚E-112˚E). Arom_op means total oxidization products of aromatics.

References

1   Tian, H. *et al.* An investigation of transmission control measures during the first 50 days of the COVID-19 epidemic in China. *Science* (2020).

2   Wang, C., Horby, P. W., Hayden, F. G. & Gao, G. F. A novel coronavirus outbreak of global health concern (vol 395, pg 470, 2020). *Lancet* **395**, 496-496, doi:10.1016/S0140-6736(20)30250-6 (2020).

3   *NASA Goddard Space Flight Center, Airborne Nitrogen Dioxide Plummets Over China*, 2020).

4   Wang, P., Chen, K., Zhu, S., Wang, P. & Zhang, H. Severe air pollution events not avoided by reduced anthropogenic activities during COVID-19 outbreak. *Resour. Conserv. Recy.* **158**, 104814 (2020).

5   Sun, Y. L. *et al.* Aerosol composition, sources and processes during wintertime in Beijing, China. *Atmos. Chem. Phys.* **13**, 4577-4592, doi:10.5194/acp-13-4577-2013 (2013).

6   Huang, R. J. *et al.* High secondary aerosol contribution to particulate pollution during haze events in China. *Nature* **514**, 218-222, doi:10.1038/nature13774 (2014).

7   Wang, Y. S. *et al.* Mechanism for the formation of the January 2013 heavy haze pollution episode over central and eastern China. *Sci. China Earth Sci.* **57**, 14-25, doi:10.1007/s11430-013-4773-4 (2014).

8   Wang, G. H. *et al.* Persistent sulfate formation from London Fog to Chinese haze. *P. Natl. Acad. Sci. USA* **113**, 13630-13635, doi:10.1073/pnas.1616540113 (2016).

9   Song, S. J. *et al.* Possible heterogeneous chemistry of hydroxymethanesulfonate (HMS) in northern China winter haze. *Atmos. Chem. Phys.* **19**, 1357-1371, doi:10.5194/acp-19-1357-2019 (2019).

10   Cheng, Y. F. *et al.* Reactive nitrogen chemistry in aerosol water as a source of sulfate during haze events in China. *Sci. Adv.* **2**, doi:10.1126/sciadv.1601530 (2016).

11   Guo, S. *et al.* Remarkable nucleation and growth of ultrafine particles from vehicular exhaust. *P. Natl. Acad. Sci. USA* **117**, 3427-3432, doi:10.1073/pnas.1916366117 (2020).

12   Zhang, Q. *et al.* Drivers of improved PM2.5 air quality in China from 2013 to 2017. *P. Natl. Acad. Sci. USA* **116**, 24463-24469, doi:10.1073/pnas.1907956116 (2019).

13   Ding, A. J. *et al.* Significant reduction of PM2.5 in eastern China due to regional-scale emission control: evidence from SORPES in 2011-2018. *Atmos. Chem. Phys.* **19**, 11791-11801, doi:10.5194/acp-19-11791-2019 (2019).

14   Lelieveld, J., Evans, J. S., Fnais, M., Giannadaki, D. & Pozzer, A. The contribution of outdoor air pollution sources to premature mortality on a global scale. *Nature* **525**, 367-+, doi:10.1038/nature15371 (2015).

15   Wang, T. *et al.* Ozone pollution in China: A review of concentrations, meteorological influences, chemical precursors, and effects. *Sci. Total Environ.* **575**, 1582-1596, doi:10.1016/j.scitotenv.2016.10.081 (2017).

16   Li, K. *et al.* Anthropogenic drivers of 2013-2017 trends in summer surface ozone in China. *P. Natl. Acad. Sci. USA* **116**, 422-427, doi:10.1073/pnas.1812168116

(2019).

17 Guo, S. *et al.* Elucidating severe urban haze formation in China. *P. Natl. Acad. Sci. USA* **111**, 17373-17378, doi:10.1073/pnas.1419604111 (2014).

18 Zhang, Y. *et al.* Impact of synoptic weather patterns and inter-decadal climate variability on air quality in the North China Plain during 1980-2013. *Atmos Environ* **124**, 119-128, doi:10.1016/j.atmosenv.2015.05.063 (2016).

19 Wang, T. *et al.* Air quality during the 2008 Beijing Olympics: secondary pollutants and regional impact. *Atmos. Chem. Phys.* **10**, 7603-7615, doi:10.5194/acp-10-7603-2010 (2010).

20 Wang, Y. *et al.* Ozone air quality during the 2008 Beijing Olympics: effectiveness of emission restrictions. *Atmos. Chem. Phys.* **9**, 5237-5251, doi:DOI 10.5194/acp-9-5237-2009 (2009).

21 Pollack, I. B. *et al.* Airborne and ground-based observations of a weekend effect in ozone, precursors, and oxidation products in the California South Coast Air Basin. *J. Geophys. Res.-Atmos.* **117**, doi:10.1029/2011jd016772 (2012).

22 Jiang, Q., Sun, Y. L., Wang, Z. & Yin, Y. Aerosol composition and sources during the Chinese Spring Festival: fireworks, secondary aerosol, and holiday effects. *Atmos. Chem. Phys.* **15**, 6023-6034, doi:10.5194/acp-15-6023-2015 (2015).

23 Xu, Z. N. *et al.* Influence of synoptic condition and holiday effects on VOCs and ozone production in the Yangtze River Delta region, China. *Atmos. Environ.* **168**, 112-124, doi:10.1016/j.atmosenv.2017.08.035 (2017).

24 Levy, I. A national day with near zero emissions and its effect on primary and secondary pollutants. *Atmos. Environ.* **77**, 202-212, doi:10.1016/j.atmosenv.2013.05.005 (2013).

25 Witte, J. C. *et al.* Satellite observations of changes in air quality during the 2008 Beijing Olympics and Paralympics. *Geophys. Res. Lett.* **36**, doi:10.1029/2009gl039236 (2009).

26 Tan, P. H., Chou, C., Liang, J. Y., Chou, C. C. K. & Shiu, C. J. Air pollution "holiday effect" resulting from the Chinese New Year. *Atmos. Environ.* **43**, 2114-2124, doi:10.1016/j.atmosenv.2009.01.037 (2009).

27 Ansari, T. U. *et al.* Effectiveness of short-term air quality emission controls: a high-resolution model study of Beijing during the Asia-Pacific Economic Cooperation (APEC) summit period. *Atmos. Chem. Phys.* **19**, 8651-8668, doi:10.5194/acp-19-8651-2019 (2019).

28 Maenhaut, W., Salma, I., Cafmeyer, J., Annegarn, H. J. & Andreae, M. O. Regional atmospheric aerosol composition and sources in the eastern Transvaal, South Africa, and impact of biomass burning. *J. Geophys. Res.-Atmos.* **101**, 23631-23650, doi:10.1029/95jd02930 (1996).

29 Cao, J. J. *et al.* Characteristics and sources of carbonaceous aerosols from Shanghai, China. *Atmos. Chem. Phys.* **13**, 803-817, doi:10.5194/acp-13-803-2013 (2013).

30 Seinfeld, J. H. & Pankow, J. F. Organic atmospheric particulate material. *Annu. Rev. Phys. Chem.* **54**, 121-140, doi:10.1146/annurev.physchem.54.011002.103756 (2003).

31   Brown, S. S. *et al.* Variability in nocturnal nitrogen oxide processing and its role in regional air quality. *Science* **311**, 67-70, doi:10.1126/science.1120120 (2006).

32   Hallquist, M. *et al.* The formation, properties and impact of secondary organic aerosol: current and emerging issues. *Atmos. Chem. Phys.* **9**, 5155-5236, doi:10.5194/acp-9-5155-2009 (2009).

33   McDuffie, E. E. *et al.* Heterogeneous N2O5 Uptake During Winter: Aircraft Measurements During the 2015 WINTER Campaign and Critical Evaluation of Current Parameterizations. *J. Geophys. Res.-Atmos.* **123**, 4345-4372, doi:10.1002/2018jd028336 (2018).

34   Kroll, J. H. & Seinfeld, J. H. Chemistry of secondary organic aerosol: Formation and evolution of low-volatility organics in the atmosphere. *Atmos. Environ.* **42**, 3593-3624, doi:10.1016/j.atmosenv.2008.01.003 (2008).

35   Brasseur, G. P., Muller, J. F. & Granier, C. Atmospheric impact of NOx emissions by subsonic aircraft: A three-dimensional model study. *J. Geophys. Res.-Atmos.* **101**, 1423-1428, doi:Doi 10.1029/95jd02363 (1996).

36   Crawford, J. *et al.* An assessment of ozone photochemistry in the extratropical western North Pacific: Impact of continental outflow during the late winter early spring. *J. Geophys. Res.-Atmos.* **102**, 28469-28487, doi:10.1029/97jd02600 (1997).

37   Lu, K. *et al.* Oxidant (O3+ NO2) production processes and formation regimes in Beijing. *J. Geophys. Res.-Atmos.* **115** (2010).

38   Edwards, P. M. *et al.* Transition from high- to low-NOx control of night-time oxidation in the southeastern US. *Nat. Geosci.* **10**, 490, doi:10.1038/Ngeo2976 (2017).

39   Ronald, J. V. *et al.* Cleaning up the air: effectiveness of air quality policy for SO2 and NOx emissions in China. *Atmos. Chem. Phys.* **17**, 1775-1789, doi:10.5194/acp-17-1775-2017 (2017).

40   Richter, A., Burrows, J. P., Nuss, H., Granier, C. & Niemeier, U. Increase in tropospheric nitrogen dioxide over China observed from space. *Nature* **437**, 129-132, doi:10.1038/nature04092 (2005).

41   Wang, Y., Zhang, Q. Q., He, K., Zhang, Q. & Chai, L. Sulfate-nitrate-ammonium aerosols over China: response to 2000-2015 emission changes of sulfur dioxide, nitrogen oxides, and ammonia. *Atmos. Chem. Phys.* **13**, 2635-2652, doi:10.5194/acp-13-2635-2013 (2013).

42   Shah, V. *et al.* Chemical feedbacks weaken the wintertime response of particulate sulfate and nitrate to emissions reductions over the eastern United States. *P. Natl. Acad. Sci. USA* **115**, 8110-8115, doi:10.1073/pnas.1803295115 (2018).

43   Shrivastava, M. *et al.* Recent advances in understanding secondary organic aerosol: Implications for global climate forcing. *Rev. Geophys.* **55**, 509-559, doi:10.1002/2016rg000540 (2017).

44   Liu, F. *et al.* High-resolution inventory of technologies, activities, and emissions of coal-fired power plants in China from 1990 to 2010. *Atmos. Chem. Phys.* **15**, 13299-13317, doi:10.5194/acp-15-13299-2015 (2015).

45   Liu, M. X. *et al.* Ammonia emission control in China would mitigate haze

pollution and nitrogen deposition, but worsen acid rain. *P. Natl. Acad. Sci. USA* **116**, 7760-7765, doi:10.1073/pnas.1814880116 (2019).

46   Liu, J. *et al.* Air pollutant emissions from Chinese households: A major and underappreciated ambient pollution source. *P. Natl. Acad. Sci. USA* **113**, 7756-7761, doi:10.1073/pnas.1604537113 (2016).

47   Li, M. *et al.* Mapping Asian anthropogenic emissions of non-methane volatile organic compounds to multiple chemical mechanisms. *Atmos. Chem. Phys.* **14**, 5617-5638, doi:10.5194/acp-14-5617-2014 (2014).

48   Zheng, B. *et al.* High-resolution mapping of vehicle emissions in China in 2008. *Atmos. Chem. Phys.* **14**, 9787-9805, doi:10.5194/acp-14-9787-2014 (2014).

Methods

Observational datasets and analysis method

Measurements on hourly concentrations of air pollutants are analyzed to understand air quality change due to the most extreme COVID-19 lockdown in China. Concentration of NO_2, O_3, CO, SO_2, $PM_{2.5}$ and PM_{10} at more than 1500 stations are recorded hourly mainly based on Thermo Scientific samplers and analyzers. The geographic locations of these station are marked in Fig. 1 (a-d). All these ground-based observations are archived at air monitoring data center of Ministry of Ecology and Environment of the People's Republic of China (http://datacenter.mep.gov.cn), which are collected to derive the spatiotemporal variations in this study. As aforementioned, we divided the first two month of 2020 into two distinct time period according to the sharp drop of transportation activities due to the hit of COVID-19. The concentration level of multiple air pollutants during Pre-COVID and COVID-lock period. To clearly demonstrate the air quality response variations, ensemble empirical mode decomposition (EEMD) is applied to decompose observational data and to derive the low frequency signals (timescale larger than 2 days).

In addition, $PM_{2.5}$ chemical compositions are recorded at more than air pollution observation network developed by environment monitoring centers in developed provinces and cities in eastern China. In Nanjing, besides routinely measured aerosol and its chemical compositions, we also conducted measurements on particle size distribution, VOC and other trace gases at the Stations for Observing Regional Processes of the Earth System (SORPES). The SORPES station is a cross-disciplinary research and experiment platform that was established in 2011 to understand the impact of human activities in the rapidly urbanized and industrialized eastern China region[13]. A scanning mobility particle sizer (SMPS), Aerodyne Soot Particle Aerosol Mass Spectrometer (SP-AMS), Time-of-Flight Aerosol Chemical Speciation Monitor (TOF-ACSM), compact IONICON PTF-TOF-MS trace VOC analyzer, and Aerodyne Research Long-Tof-CIMS were used to measure aerosol size distribution, fine particle chemical compositions, VOCs speciation, and sulfuric acid, respectively, at the station.

TROPOspheric Monitoring Instrument (TROPOMI) on board the Copernicus Sentinel-5 Precursor satellite provides retrievals of NO_2 column amount[49], which are also employed to illustrate the spatial pattern and temporal variation of pollution in China during COVID-19 lockdown. The retrieved column burden is then averaged and compared in different regions for Pre-COVID and COVID-lock period.

Emission reduction estimation due to the lockdown control

Emission reduction is estimated using the bottom-up inventory model of Multi-resolution Emission Inventory for China (MEIC), developed by Tsinghua University4[47]. The MEIC model uses the technology-based approach calculating air pollutant emissions from more than 700 anthropogenic sources in China, which can be categorized into five source sectors: power, industry, residential, transportation, and agriculture. The most up-to-date version provides China's anthropogenic emissions

data until the year 2019.

To estimate emission reductions due to COVID-19 lockdown, we update China's emissions data to Jan and Feb 2020 based on dynamic economic and industrial activity levels. The thermal power generation in the first two months of 2020 was 8.9% lower than that in 2019, while China generated 1.7% more thermal power in January and February 2019 than in 2018 (Natural Bureau of Statistics, http://www.stats.gov.cn). We then assume that the difference in the growth rates between 2019 and 2020 was the influence of COVID-19 lockdown on the power sector emissions. The same approach is applied to the industrial sector. For example, cement production in January and February 2020 was 29.5% lower than that in 2019, while China produced 0.5% more cement in January and February 2019 than in 2018. Cement emissions were then estimated to be reduced by 30% due to COVID-19. For the residential sector, emissions from the commercial use of boilers and stoves in the urban region were eliminated since the lockdown measure implemented, while emissions from residential heating and cooking in both urban and rural areas were assumed not affected. For the transport sector, decline in national traffic volume was estimated at 70% during the COVID-19 lockdown, according to the transportation index data. Activity level of off-road equipment such as construction machines was assumed approaching zero during the COVID-19 lockdown. As the result, on-road emissions declined by 70%, and the off-road emissions became zero during the lockdown. The detailed estimation of provincial emission reduction ratio of main trace gases and primary PM are presented in Extended Data Table 1. Evaluation of WRF-Chem simulations based on this inventory are given in Extended Data Fig. 6.

Regional air quality modeling

To quantitatively understand the response of air quality, regional coupled dynamical and chemical simulations are conducted based on WRF-Chem model (Weather Research and Forecasting model coupled with Chemistry, version 3.7.1). WRF-Chem model is a state-of-the-art meteorology/chemistry model developed that includes a variety of coupled physical and chemical processes such as emission and deposition of pollutants, advection and diffusion, gaseous and aqueous chemical transformation, aerosol chemistry and dynamics, etc[50]. The model has been widely used and evaluated against measurements, which has been further improved by optimizing parametrization of aqueous and heterogeneous chemistry in Asia[51]. The model domain with a grid resolution of 20 km covered the eastern China and its surrounding areas to get synoptic forcing. There are 30 vertical layers from the ground level to the top pressure of 50 hPa, in which more than ten layers are settled under 1 km to better describe boundary layer processes. The simulation is conducted from 1 December 2019 to 5 March 2020. The initial and boundary meteorological conditions were the NCEP global final analysis (FNL) data. NCEP Automated Data Processing (ADP) surface and global upper air observational weather data of wind, temperature and moisture is assimilated to better characterize the regional transport pattern of air pollution. The Yonsei University planet boundary layer (YSU PBL) scheme is applied to parameterize the boundary layer processes in this simulation. Other key parameterization options are the Noah land

surface scheme to describe the land-atmosphere interactions, the Lin microphysics scheme with the Grell cumulus parameterization to reproduce the cloud and precipitation processes, and the RRTMG short- and long-wave radiation scheme. For the numerical representation of atmospheric chemistry, Carbon-Bond photochemical mechanism combined with MOSAIC (Model for Simulating Aerosol Interactions and Chemistry) aerosol module.

Both natural and anthropogenic emissions were included for the regional WRF-Chem modeling in the present work. MEGAN (Model of Emissions of Gases and Aerosols from Nature) module embedded in WRF-Chem model is used to calculate biogenic emissions online. It estimates the net emission rates of isoprene, monoterpene and other biogenic VOCs from terrestrial ecosystems into the above-canopy atmosphere. Soil-derived dust emission is characterized by GOCART emission schemes. Anthropogenic emissions from power plants, residential combustion, industrial processes, on-road mobile sources and agricultural activities were derived from the MEIC, which is described above. Emissions outside China was obtained from the MIX Asian emission inventory [52]. We then use the up-to-date emission reduction ratio considering the activity level change due to COVID lockdown, as mentioned above, to quantitatively understand the emission-triggered perturbations in air pollution. Furthermore, a number of WRF-Chem simulations are carried out based on different emission scenarios with a series of NOx and VOC emission.

Data availability

All the observation and simulation data that support the findings of this study are available at Figshare data publisher. Daily satellite retrievals of NO_2 column amount are openly accessible at http://www.temis.nl/airpollution/no2col/data/tropomi. The daily transportation index is provided by Baidu migration dataset (https://qianxi.baidu.com). The simulation data used in this study are stored on high performance computing center of Nanjing University and can be made available from the corresponding author upon request.

Code availability

Data processing techniques are available on request from the corresponding author. The source code of WRF-Chem model is archived on UCAR data repository (http://www2.mmm.ucar.edu/wrf/users/download).

Acknowledgements

Monitoring Centers of cities in eastern China for their contributions on the field measurements.

Author Contributions.

A.D, X.H., Q. Z. and K.H. conceived the study and led the overall scientific questions. X. H and A.D. made the data analysis and modeling studies. J. G., F. C., Q. Fu and W. Q. collected and processes the chemical composition measurement data. B. Z. and D.T. developed the base year emission inventory and estimated emission reduction during the COVID-19 lockdown. X. H., A.D., Q. Z. and S.D. wrote the paper with contribution from all coauthors.

Competing interests

The authors declare no competing interests.

Correspondence and requests for materials should be addressed to A. D. (dingaj@nju.edu.cn.) or Q. Z. (qiangzhang@tsinghua.edu.cn).

References:

49   Veefkind, J. *et al.* TROPOMI on the ESA Sentinel-5 Precursor: A GMES mission for global observations of the atmospheric composition for climate, air quality and ozone layer applications. *Remote. Sens. Environ.* **120**, 70-83 (2012).

50   Grell, G. A. *et al.* Fully coupled "online" chemistry within the WRF model. *Atmos. Environ.* **39**, 6957-6975 (2005).

51   Huang, X. *et al.* Pathways of sulfate enhancement by natural and anthropogenic mineral aerosols in China. *J. Geophys. Res.-Atmos.* **119**, 14165-14179, doi:10.1002/2014jd022301 (2014).

52   Li, M. *et al.* MIX: a mosaic Asian anthropogenic emission inventory under the international collaboration framework of the MICS-Asia and HTAP. *Atmos. Chem. Phys.* **17**, 935-963, doi:10.5194/acp-17-935-2017 (2017).

Extended Data Table 1 | Estimation of provincial emission reduction ratio (%) of CO, NOx, SO₂, VOC, PM2.5, BC, OC due to COVID-19 lockdown in China.

| Province	CO	NOx	SO₂	VOC	PM$_{2.5}$	BC	OC
Beijing	22%	45%	26%	45%	18%	46%	8%
Tianjin	21%	38%	20%	41%	14%	22%	6%
Hebei	15%	45%	16%	36%	12%	17%	5%
Shanxi	18%	40%	20%	33%	16%	19%	10%
Inner Mongolia	14%	29%	15%	34%	13%	16%	6%
Liaoning	21%	40%	28%	36%	16%	28%	8%
Jilin	16%	39%	23%	34%	13%	18%	5%
Heilongjiang	17%	37%	27%	28%	13%	15%	7%
Shanghai	35%	48%	42%	45%	34%	54%	42%
Jiangsu	23%	50%	26%	41%	16%	35%	7%
Zhejiang	41%	50%	29%	45%	30%	49%	20%
Anhui	14%	56%	22%	31%	11%	22%	4%
Fujian	29%	51%	30%	42%	19%	31%	7%
Jiangxi	24%	53%	21%	43%	19%	30%	9%
Shandong	23%	50%	25%	39%	19%	35%	9%
Henan	23%	57%	22%	41%	18%	35%	8%
Hubei	19%	55%	23%	35%	16%	23%	10%
Hunan	22%	51%	25%	36%	20%	24%	15%
Guangdong	38%	50%	33%	46%	27%	42%	13%
Guangxi	24%	50%	28%	39%	17%	27%	5%
Hainan	24%	44%	25%	36%	14%	25%	4%
Chongqing	18%	53%	32%	37%	14%	20%	4%
Sichuan	16%	50%	27%	33%	9%	15%	3%
Guizhou	24%	39%	25%	30%	22%	25%	20%
Yunnan	24%	51%	25%	41%	18%	21%	8%
Tibet	16%	35%	15%	35%	14%	14%	5%
Shaanxi	19%	45%	18%	34%	13%	22%	5%
Gansu	13%	47%	16%	29%	9%	13%	3%
Qinghai	23%	46%	22%	39%	20%	20%	7%
Ningxia	24%	36%	24%	39%	20%	23%	8%
Xinjiang	16%	35%	15%	35%	14%	14%	5%
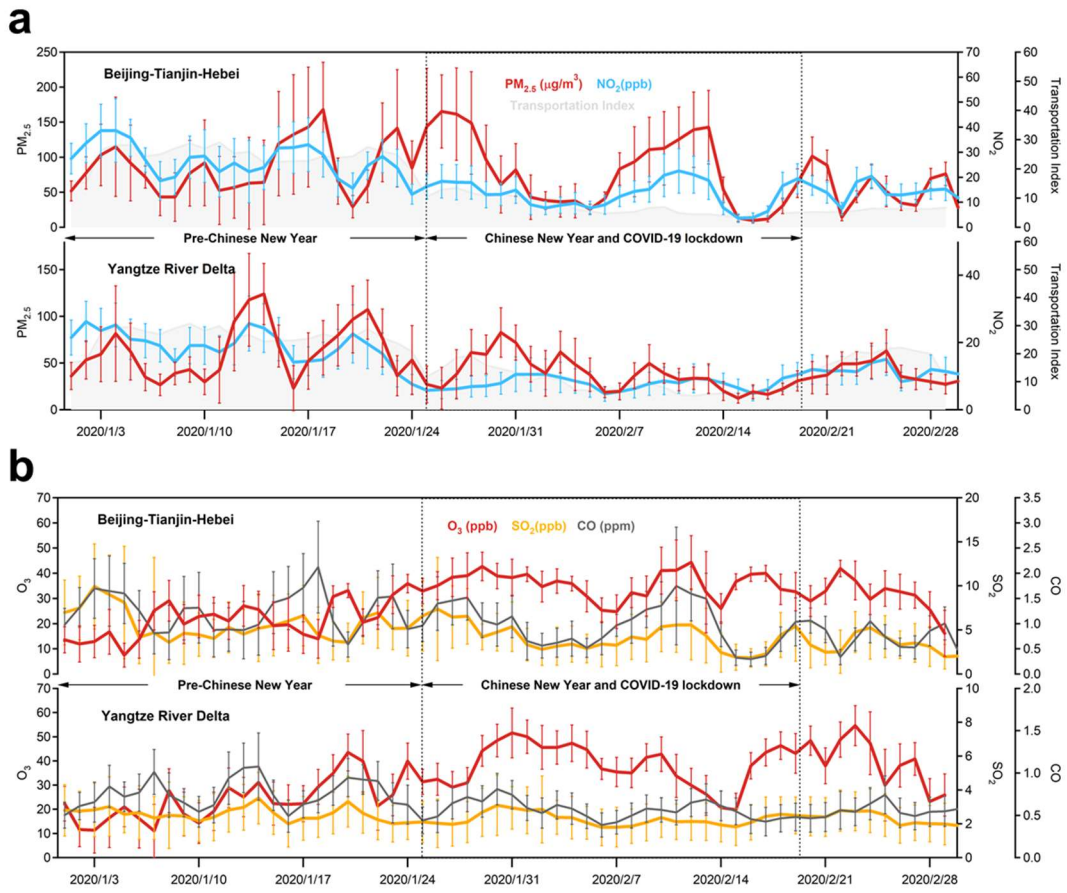
Extended Data Fig. 1 | Air quality before and during the COVID-19 epidemic in eastern China. a, Time series of daily $PM_{2.5}$, NO_2 and transportation index in the BTH (upper panel) and the YRD (lower panel) during January-February 2020. **b,** Time series of daily O_3, SO_2, and CO in the BTH (upper panel) and the YRD (lower panel) during January-February 2020.
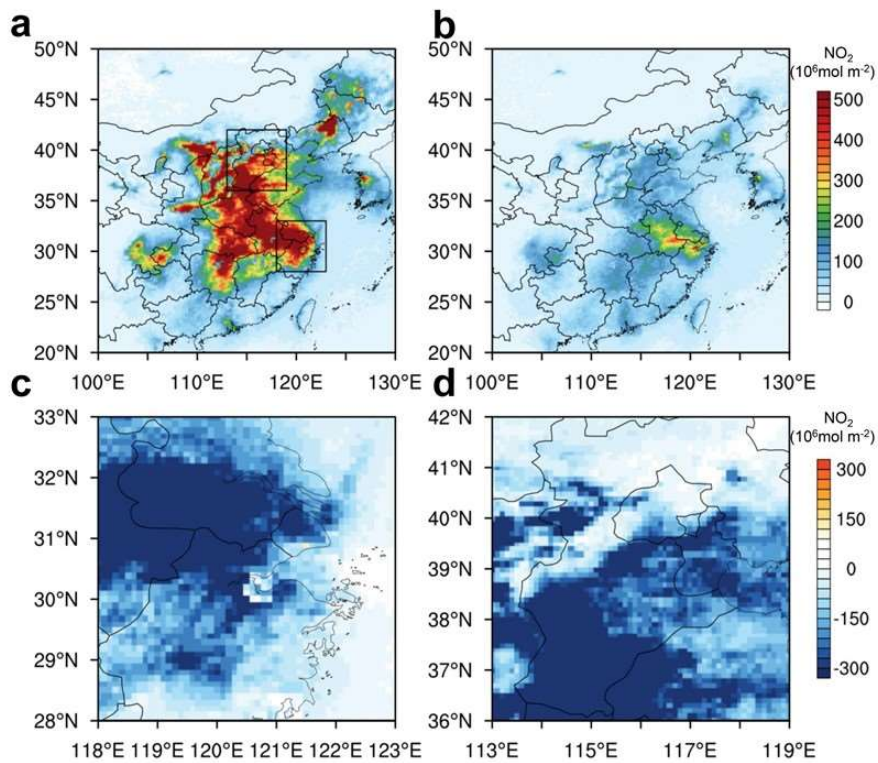
Extended Data Fig. 2 | Satellite retrievals of NO₂ in eastern China before and during the COVID-19 epidemic. a-b, Spatial distribution of averaged Trop-OMI tropospheric NO₂ column in eastern China during the pre-COVID and COVID-lock periods. **c-d,** changes in Trop-OMI tropospheric NO₂ column in the BTH and YRD regions.
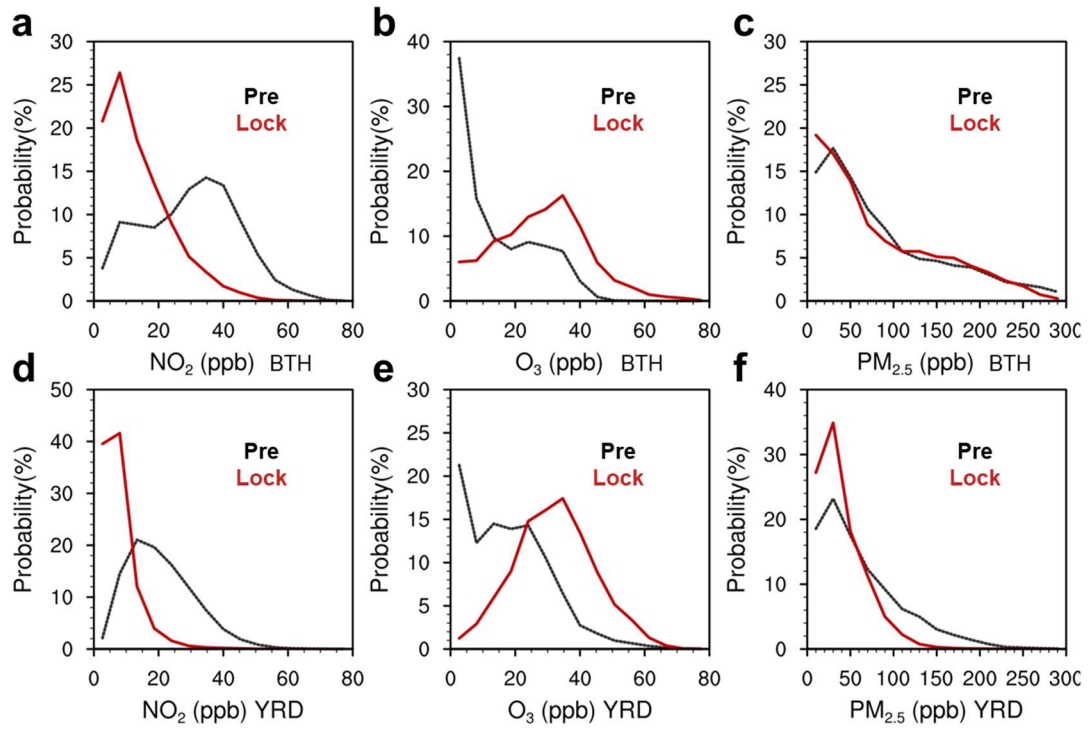
Extended Data Fig. 3 | Comparison of frequency distribution of air pollutants in eastern China due to COVID-19 lockdown. a-c, Normalized frequency distributions of NO_2, O_3, and $PM_{2.5}$ in the BTH region during the COVID-lock (red lines) and pre-COVID (black lines) periods. **d-f,** Normalized frequency distributions of NO_2, O_3, and $PM_{2.5}$ in the YRD region.
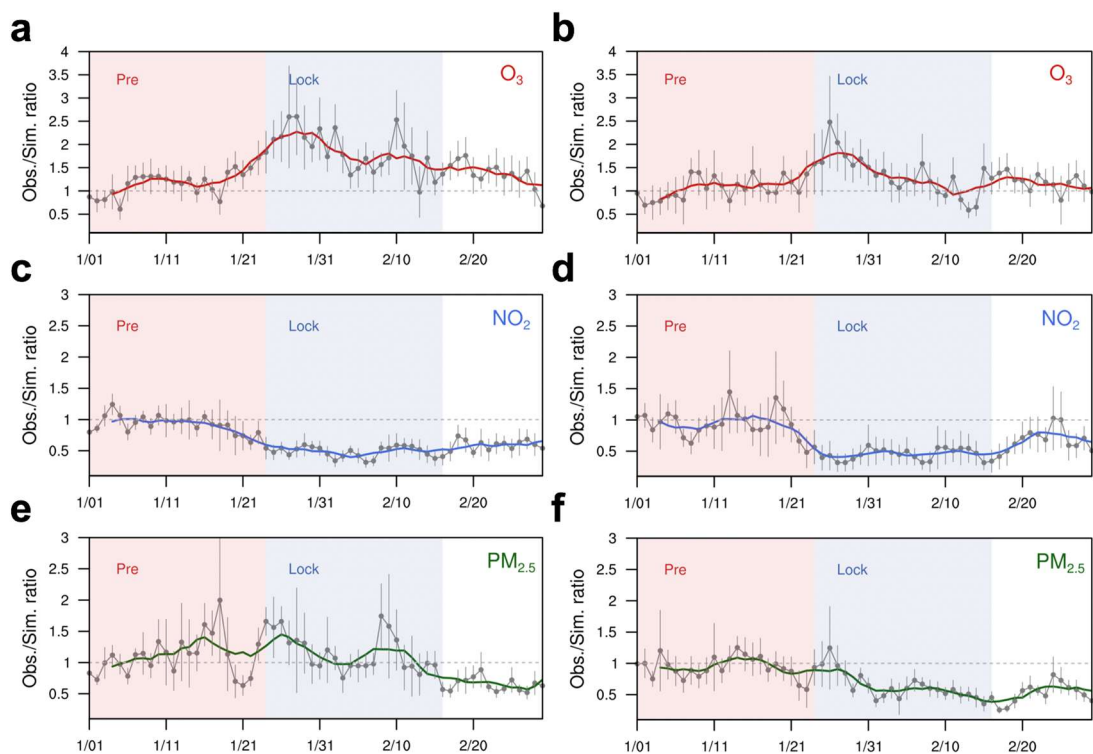
Extended Data Fig. 4 | Changes in air pollution indicated by comparison between observation and simulations. a, b, Time series of daily ratio of observation verse WRF-Chem simulated O_3 with fixed emission inventory in the BTH and YRD region. **c,d,** same as **a** and **b** but for NO_2. **e.f,** same as **a** and **b** but for $PM_{2.5}$.
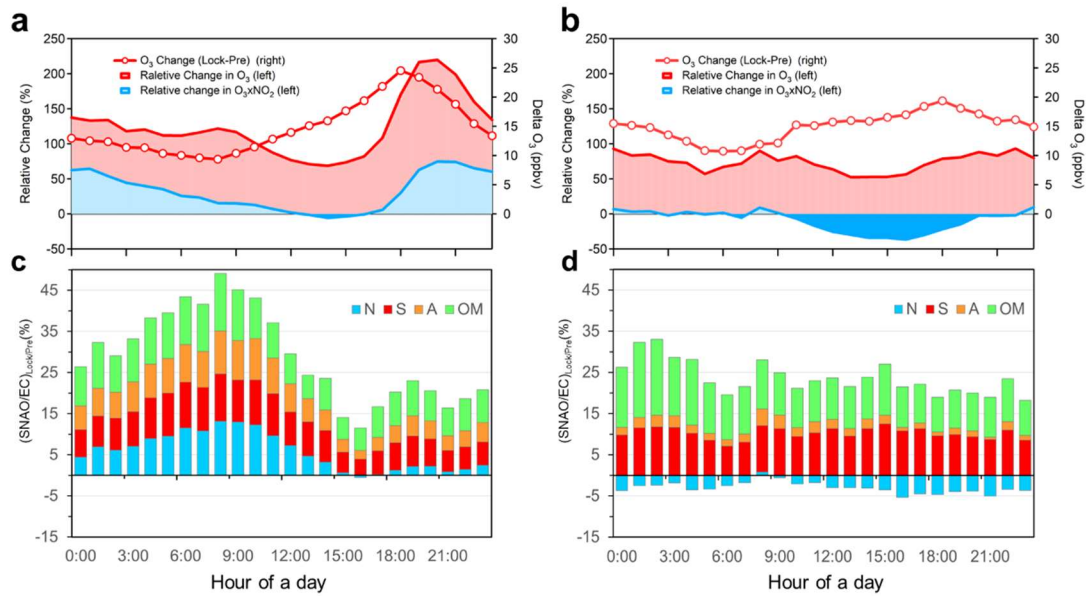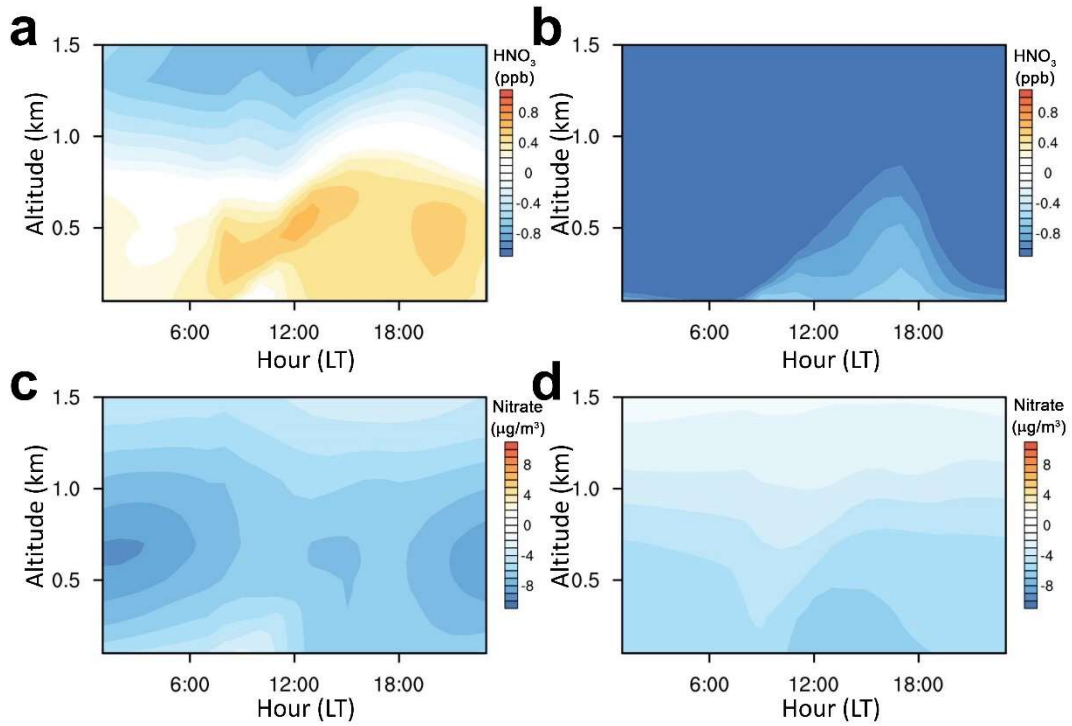
Extended Data Fig. 5 | Diurnal cycle of secondary verse primary PM₂.₅ ratio and changes in O₃ and NO₃ proxy in BTH and YRD. a, b, Changes in O_3 and O_3*NO_2 proxy between the COVID-lock and pre-COVID periods in BTH and YRD. **c, d,** changes in SNAO/EC ratio between the COVID-lock and pre-COVID periods in BTH and YRD. Note: N, S, A and OM means nitrate, sulfate, ammonium and organic matter, respectively.
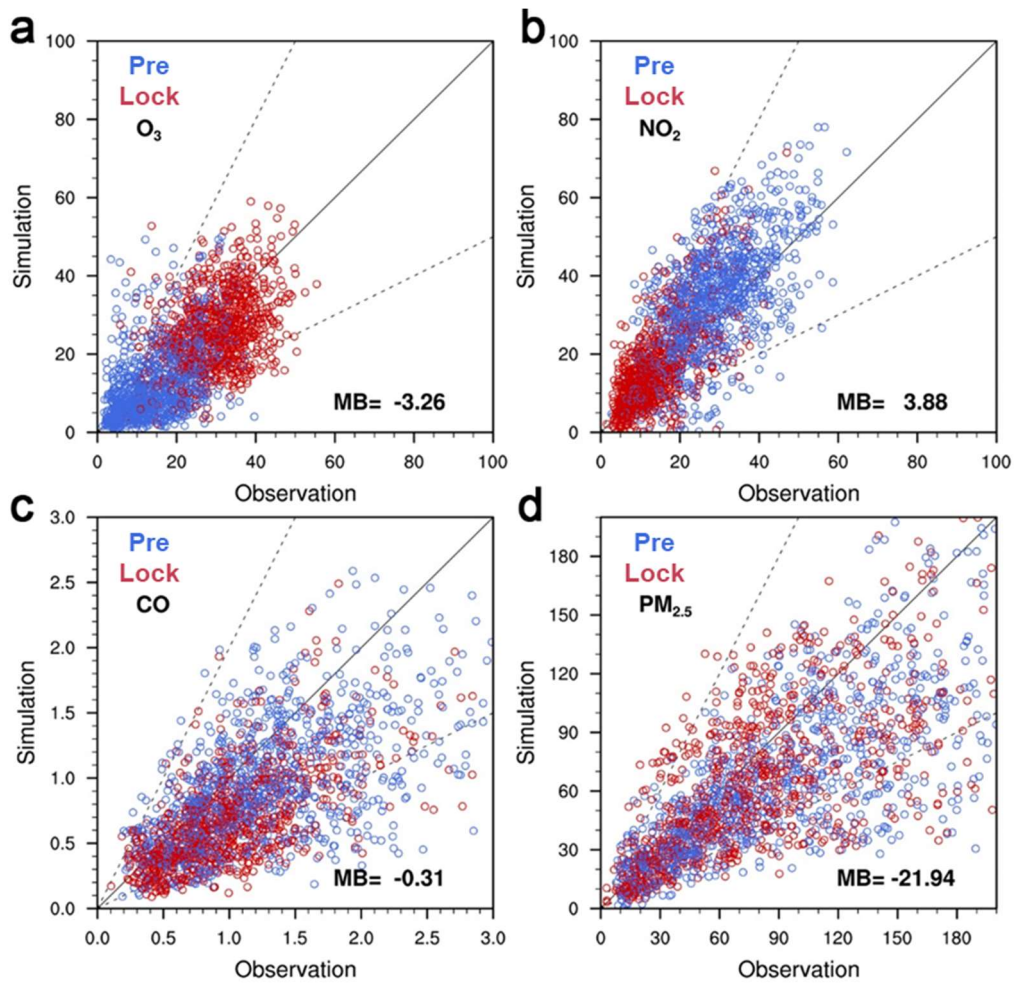
Extended Data Fig. 6 | Evaluation of WRF-Chem simulations with ambient measurements by the national air quality monitoring networks. a-d, Scatter plots of simulation verse observation for O_3, NO_2, CO and $PM_{2.5}$. Note that the blue and red markers present simulations and observations during the COVID-lock and pre-COVID periods, respectively. Mean bias of modeled concentrations are labeled in the bottom right corner of each subplot.
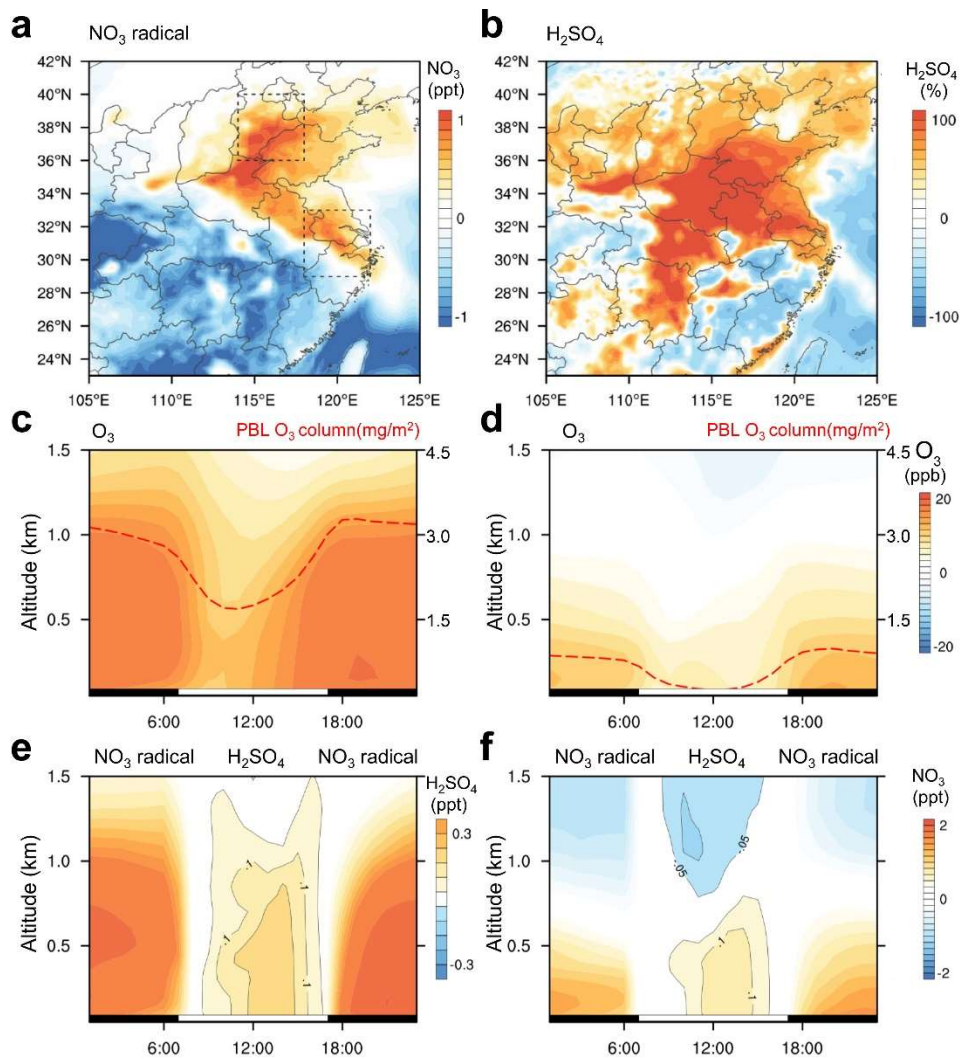
Extended Data Fig. 7 | Modeling evidences of enhanced oxidization capacity during the COVID-19 lockdown period in BTH and YRD, China. a-b, Spatial distribution of averaged changes in NO_3 radical and H_2SO_4 between the COVID-lock and pre-COVID periods (Ctrl minus Pre) in BTH and YRD, China. **c, d**, Diurnal cycle of averaged vertical distribution of O_3 and boundary layer (0-1 km) O_3 column between the two period in BTH and YRD. **e,f,** Diurnal cycle of NO_3 radical and H_2SO_4 between the two period in BTH and YRD. Note: The black and white bar near the x axis in **c-f** indicates the nighttime and daytime of a day.

Extended Data Fig. 8 | Comparison of simulated diurnal cycles of vertical distribution of HNO₃ and nitrate in BTH and YRD. a, b, WRF-chem simulated changes in diurnal cycle of HNO₃ vertical distribution in BTH and YRD. **c,d,** same as **a** and **b** but for nitrate.
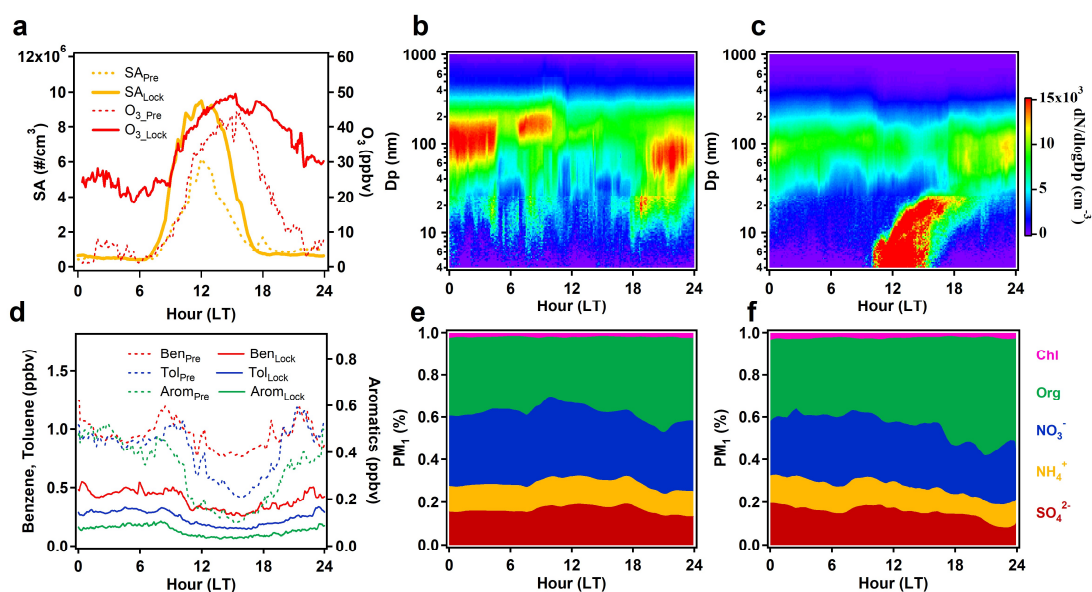
Extended Data Fig. 9 | Observations of trace gases and aerosols at the SORPES station in Nanjing during the pre-COVID and COVID-lock periods. a, Diurnal cycle of O_3 and sulfuric acid (SA) during the two periods. **b-c,** Diurnal cycle of aerosol size during pre-COVID and COVID-lock periods. **d,** Diurnal cycles of VOCs species at the SORPES station. (Ben- Benzene, Tol-Toluene, Arom- C8-C10 aromatics). **e-f,** Diurnal cycles of percentage of PM_1 speciation the pre-COVID and COVID-lock periods.
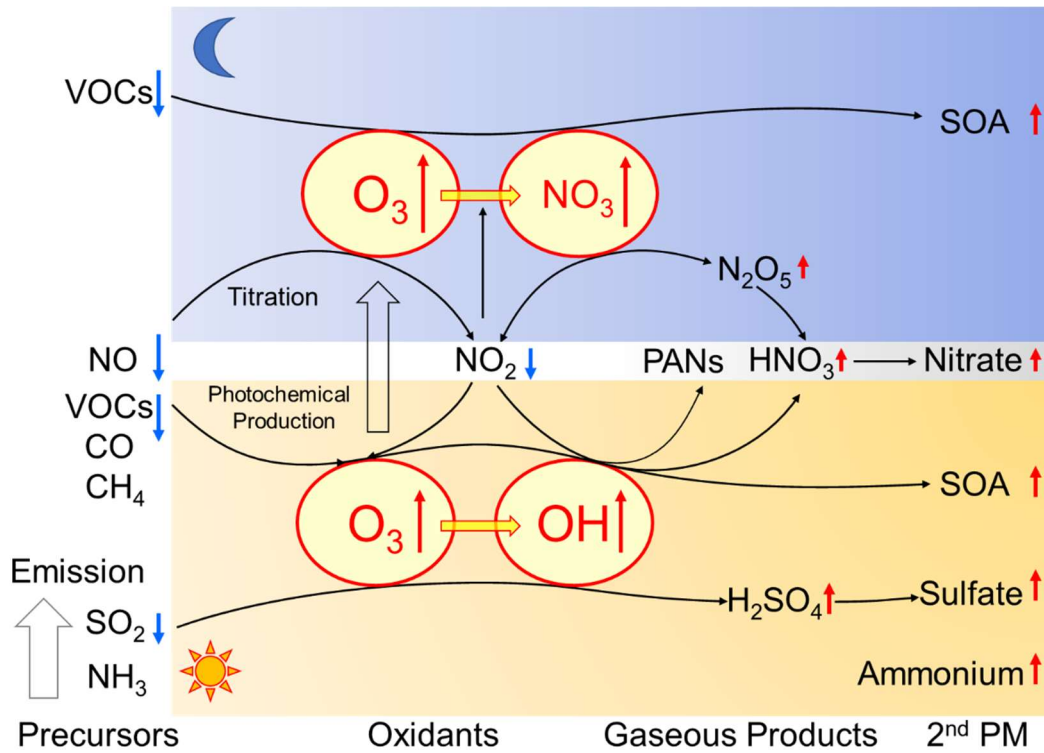
Extended Data Fig. 10 | Conceptual model showing how secondary formation offsets the reduction of primary pollutions in China with different processes during the day and night. Note: The upper and lower panels, indicated by moon and sun, represent nighttime and daytime processes, respectively. Blue downward arrows mean the reduction of emission or decrease of concentrations in the atmosphere, while the red upward arrows mean enhancement of production in the atmosphere. The length of these arrows indicated the degree of change.
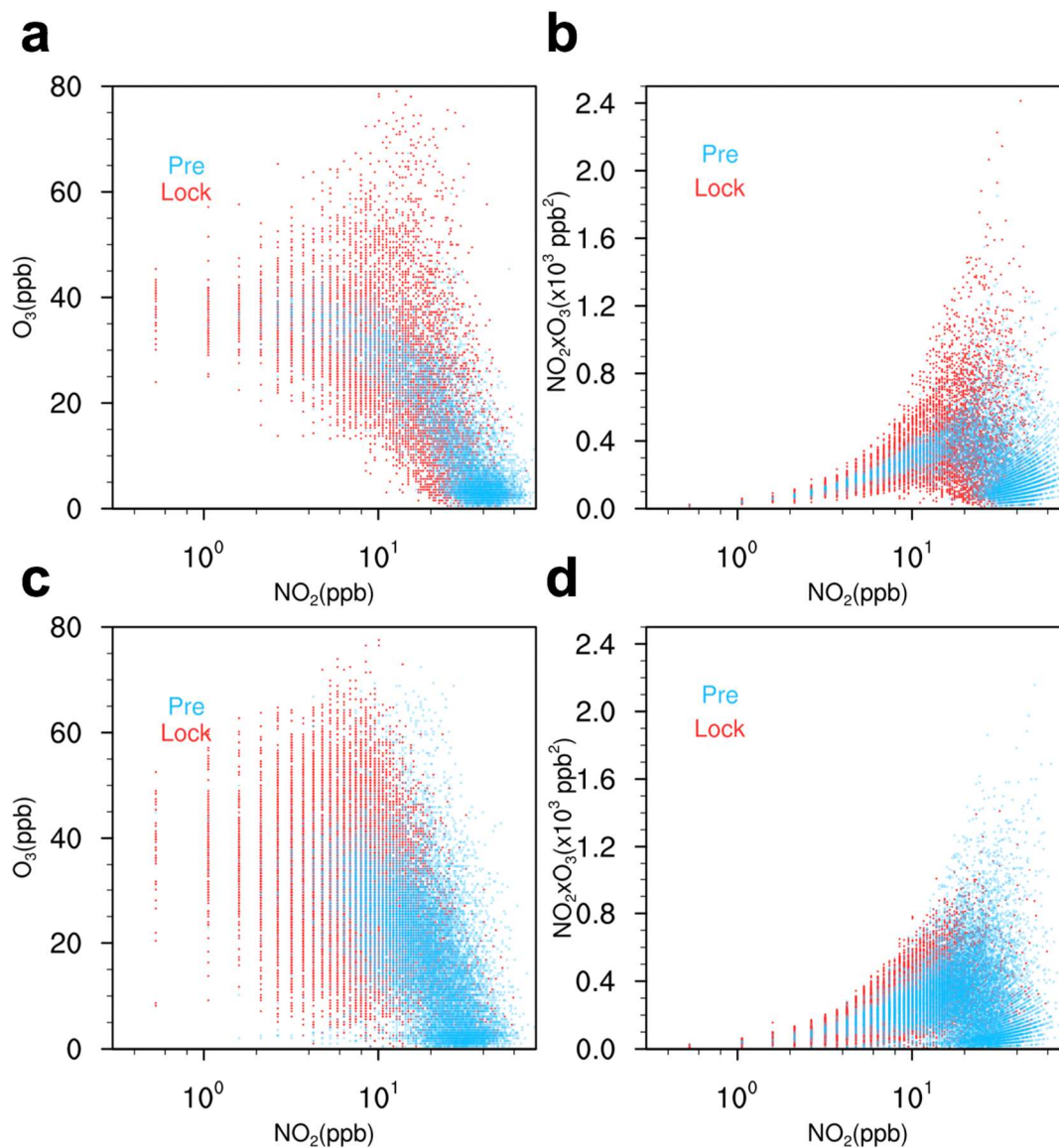
Extended Data Fig. 11 | Observed non-linear relationship between main oxidants and NO₂ caused by the COVID-19 lockdown in China. a, b, Scatter plots of O_3 and proxy of NO_3 radical (NO_2*O_3) verse NO_2 between the COVID-lock and pre-COVID periods in BTH of China. **c, d,** Same as **a** and **b** but for the YRD region.
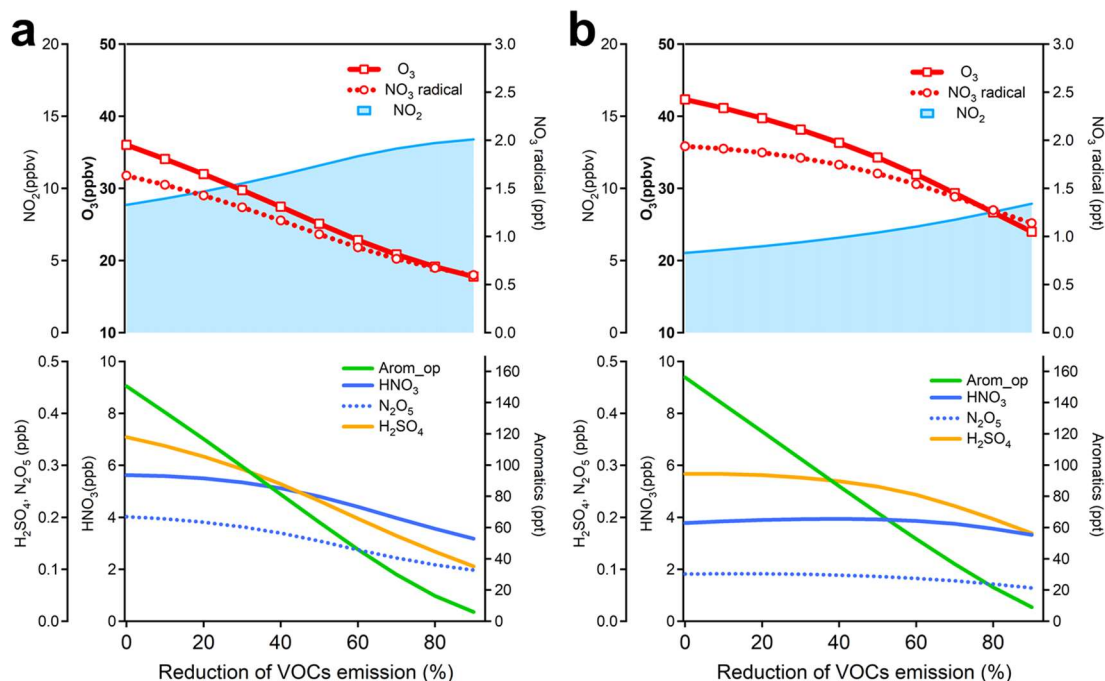
Extended Data Fig. 12 | Response of oxidization capacity to VOCs emission reductions in the BTH and YRD, China. a, b, Changes of NO_2, O_3, and NO_3 radical (upper panel) and gaseous products (proxy) (lower panel) as a function of emission reductions (NOx: 50%, VOCs: 10-90%) in the BTH and YRD regions, respectively. Note: BTH and YRD are defined as the domains of (36˚N-40˚N, 114˚E-118˚E) and (29-33˚N, 118˚E-112˚E). Arom_op means total oxidization products of aromatics.